Effect of different typical high speed train pantograph recess configurations on aerodynamic noise

Journal Title
XX(X):1–13

DOI: 10.1177/ToBeAssigned
www.sagepub.com/
SAGE

Hogun Kim[1], Zhiwei Hu[2] and David Thompson[2]

Abstract

For high-speed trains, the aerodynamic noise becomes an essential consideration in the train design. The pantograph and pantograph recess are recognised as important sources of aerodynamic noise. This paper studies the flow characteristics and noise contributions of three typical high-speed train roof configurations, namely a cavity, a ramped cavity and a flat roof with side insulation plates. The Improved Delayed Detached-Eddy Simulation approach is used for the flow calculations and the Ffowcs Williams & Hawkings aeroacoustic analogy is used for far-field acoustic predictions. Simulations are presented for a simplified train body at 1/10 scale and 300 km/h with these three roof configurations. In each case, two simplified pantographs (one retracted and one raised) are located on the roof. Analysis of the flow fields obtained from numerical simulations clearly shows the influence of the train roof configuration on the flow behaviour, including flow separations, reattachment and vortex shedding, which are potential noise sources. A highly unsteady flow occurs downstream when the train roof has a cavity or ramped cavity due to flow separation at the cavity trailing edge, while vortical flow is generated by the side insulation plates. For the ramped cavity configuration, moderately large pressure fluctuations appear on the cavity outside walls in the upstream region due to unsteady flow from the upstream edge of the plate. The raised pantograph, roof cavity, and ramped cavity are identified as the dominant noise sources. When the retracted pantograph is located in the ramped roof cavity, its noise contribution is less important. Furthermore, the insulation plates also generate tonal components in the noise spectra. Of the three configurations considered, the roof cavity configuration radiates the least noise at the side receiver in terms of A-weighted level.

Keywords

High-speed train, Aeroacoustics, Pantograph, Pantograph recess, Cavity flow

Introduction

High-speed train noise increases considerably as the speed increases; therefore, noise control has become an important aspect to consider in high-speed train design. It has been found that aerodynamic noise becomes dominant when the train speed exceeds a transition speed, which depends on the train design and track conditions, and is generally believed to be around 300 km/h for modern high-speed trains[1,2]. The pantograph and the pantograph recess are recognised as important contributors to aerodynamic noise for high-speed trains[1–4]. Compared with other aerodynamic noise sources, such as the bogies and inter-coach gaps, noise from the pantographs and their recess is more difficult to shield by conventional noise barriers due to their location at the top of the train.

Several investigations have been carried out on the noise generation mechanisms and reduction of the noise from pantographs and their recess[5–8]. Lölgen[5] carried out measurements in a wind tunnel on three on full-scale pantographs. For the DSA350SEK pantograph, he found three peaks, at 550 Hz, 900 Hz and 3500 Hz at 330 km/h, in the noise spectrum. These tonal peaks were associated with the contact strip, the pantograph horn and the stroke limiting cage, respectively. Grosche *et al.*.[6] also performed measurements for a full-scale DSA350 pantograph in a wind tunnel to obtain its noise source distribution, and identified three areas of the pantograph as main noise sources: the foot region, the panhead and the knee connector.

Noger[7] investigated aerodynamic and acoustic characteristics of a TGV pantograph recess using a 1/7 scale model. It was found that the main noise source is located in a region near the trailing edge of the cavity and interactions between the wake of the pantograph and the shear layer at the downstream region of the recess produced a lower turbulence intensity at the downstream edge than for the recess without the pantograph. Furthermore, this study indicated that a shield installed on the side of the recess reduced broadband noise. Kurita *et al.*[8] conducted field tests for a full-scale train using an spiral microphone array in order to compare Z-shaped noise insulation plates with conventional plates on a Japanese high-speed train, and showed that the strongest noise sources were at the front and rear edges of the plates as

[1]Faculty of Engineering and Physical Sciences, The University of Southampton, UK
[2]Faculty of Engineering and Physical Sciences, The University of Southampton, UK
[2]Institute of Sound and Vibration Research, The University of Southampton, UK

Corresponding author:
Hogun Kim, Faculty of Engineering and Physical Sciences, The University of Southampton, University Road, Southampton, SO17 1BJ, UK.
Email: hk1g14@soton.ac.uk

well as around the pantograph head. Tests also showed that insulation plates with ends with a 45 degree angle instead of vertical ends reduced the noise from the edges of the plates compared with the initial Z-shaped plates. They also conducted a wind tunnel test using a 1/10 scale model to optimise the edge shape of conventional insulation plates as well as the shape of its cross-section. As a result of the optimisation, insulation plates with ends with a 45 degree angle achieved a 2 dB reduction of noise compared with the original conventional insulation plates.

High-speed train aerodynamic noise studies so far have focused mainly on the pantograph itself including the pan-head and arms, the train nose or the bogie region although the noise from the pantograph recess is also of importance[4]. By comparison, much less attention has been given to the generation of aerodynamic noise from the pantograph recess. Furthermore, there is a lack of studies about the effect of the common train recess types (cavity, ramped cavity, and flat roofs) with side insulation plates on both the folded and the raised pantographs and its flow characteristic and noise generation mechanism. This paper aims to provide insight into the aerodynamic phenomena and noise generation mechanisms from three different types of pantograph roof configuration with cavity and side insulation plates and their effect on the flow around the pantograph and the radiated noise. The results from the three different roof configurations are analysed and compared, using computational methods. The Improved Delayed Detached-Eddy Simulation (IDDES) approach is used for flow simulation, combined with the Ffowcs Williamsa & Hawkings (FW-H) method for noise prediction.

The methodologies employed are introduced first, including the turbulence modelling approach and the acoustic analogy. Then, the train roof geometries and by the computational set-up are described. The results are presented in terms of the computational aerodynamics results, and then the aeroacoustic results.

Methodology

Modern high-speed trains are operated at running speeds generally around 300 km/h and in some cases up to 350 km/h, which corresponds to a Mach number of 0.3. At these speeds, the flow can be approximately treated as incompressible[9]. The unsteady incompressible Navier-Stokes equations are solved using computational fluid dynamics methods.

The simulations were performed using the commercial code, STAR-CCM+. The three-dimensional Navier-Stokes equations were solved with the Improved Delayed Detached-Eddy Simulation (IDDES) turbulence model[24–26]. The DES method has some limitations within the attached boundary layer and unsteady turbulent structure development between the URANS and LES model. This issue produces early separations, a so-called grid-induced separation[23]. As a result, the DES method has been improved by Spalart et al.[24] leading to the Delayed Detached Eddy Simulation (DDES). It has also limitation that DDES may cause logarithmic-layer mismatch[26]. Shur[26] introduced Improved DDES (IDDES) in order to solve this problem by using a new subgrid length-scale which is combining the DDES and the Wall-Modeled LES length scales. This model for turbulent content inflow allows WMLES mode to be activated within the boundary layers. These advantages lead to its use in the current study.

The Ffowcs Williams & Hawkings (FW-H) formulation is used to obtain the far-field acoustic pressure based on equivalent sources obtained from the time-resolved aerodynamic near-field data. The quadrupole term is neglected in this study because its contribution can be considered negligible for low Mach number flow[10–19,19–22]. Several authors[19–22] successfully validated numerical calculation without including the volume term compared with experimental data at low Mach numbers. This allows the integration surfaces to be selected as the solid surfaces which has significant advantages is limiting the mesh size and avoiding pseudo noise[14,15]. Therefore, only the dipole term is considered which based on Farassat's formulation 1A[30,31]. It is note that the current method for prediction of far-field pressure is not taken into account the acoustic shielding and diffraction effects of the side insulation plates.

Computational setup

Geometry

A simplified 1/10 scale high-speed train model with two pantographs (a front retracted and a rear raised) is used to reduce the complexity and computational resource requirements. Three different roof configurations are represented by the three cases illustrated in Figure 1. The first (Figure 1(a)) is a flat roof with a pantograph recess, modelled as a rectangular cavity, which is the most widely used configuration for different trains, such as TGV (France). The ramped roof cavity type (case 2, Figure 1(b)) was developed in Japan to shield noise from the pantograph, and used for Shinkansen 500 (Japan) and HEMU-430X (Korea). Case 3 shown in Figure 1(c) models trains with side insulation plates which are also commonly used in Japan and China, such as Shinkansen E5 (Japan) and CRH 380A (China). However, the geometries used here do not represent any particular train.

The pantograph cavity is simplified as a rectangular cavity with dimensions L = 0.812 m (length), D = 0.07 m (depth) and W = 0.27 m (width), giving L/D = 11.5, W/D = 3.9. For cases 2 and 3, the side insulation plates have an angle of 30 degrees at both ends as shown in Figure 1(b) and 1(c). For case 3, the height of the side insulation plates is the same as the cavity depth in cases 1 and 2. The DSA 350 pantograph model is used for the current study, as shown in Figure 1(d). Most of the pantograph components are retained apart from the small ones such as straps, springs and wire arms as listed in Table 1. The origin of the coordinate system is at the cavity leading edge and outside insulation plate.

Solver and numerical setup

The computational domain, as shown in Figure 2, extends $57D$, $30D$, and $16.5D$ in the streamwise (x), vertical (y) and spanwise (z) directions, respectively. The upstream length of the train roof is set to $20D$, which is similar to the actual length in a high-speed train from the nose to the first pantograph recess, and the downstream length is $25.5D$. The outlet and top boundaries are sufficiently far

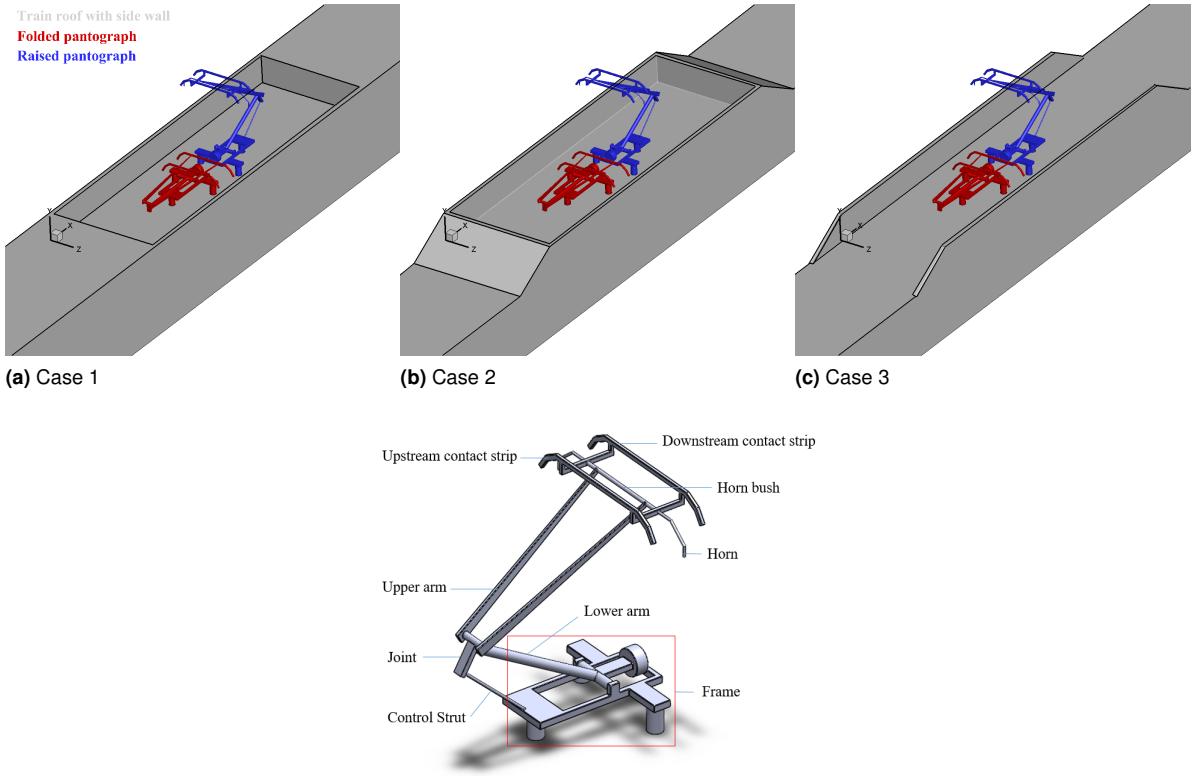

(a) Case 1 **(b)** Case 2 **(c)** Case 3

(d) Overview of the raised pantograph

Figure 1. Description of the geometry.

Table 1. List of retained and omitted parts of pantograph

Regions	Retained parts	Omitted parts
Panhead	Contact strip, horn bush, horn	Straps, head lowering, spring,
Upper arm	Upper arm, knee joint	Guide head, wire arms
Lower arm	Lower arm, control strut	

away from the cavity and the pantograph in order to have negligible effect on the flow. The cavity, the pantograph, the plate and the train body surfaces are defined as no-slip wall conditions, whereas the bottom surface is set to be a slip wall boundary with the same velocity as the inflow to model the moving ground. Symmetry boundary conditions are applied to the top and the spanwise sides of the domain. The outlet boundary is set be a pressure outlet. A velocity inlet is applied as inflow. The simulation is performed for a flow speed of 83.3 m/s (300 km/h). A hexa-dominated mesh (called trimmed mesh in STAR-CCM+) is used for all cases, generated by the STAR-CCM+ mesh generator with several refinement zones. Different cell sizes are applied for each refinement zone as summarised in Table 2 and shown in Figure 2(b). Ten different refinement zones for the cavity and the side wall regions are used. Furthermore, 38 refinement regions are used for the pantographs, including regions around all components and in the wake of the panhead and the arms of the raised pantograph. The cavity downstream and trailing edge regions are refined with a minimum cell size of 1.2 mm, the panhead region is refined to 0.4 mm, while the size for the insulation plate edge regions is 2 mm. All refinement regions have a surface growth rate of 1.1. Furthermore, 14 - 40 prism layers are used to resolve the boundary layer near solid surfaces. The first layer non-dimensional wall distance y^+ ($y_1^+ \equiv \frac{u_* y}{\nu}$, where u_* is the friction velocity, y_1 is the distance of the first grid point to the wall, and ν is the kinematic viscosity) is smaller than 1.0 and a grid stretching ratio of 1.12 in the wall normal direction is used. A non-dimensional time step $U\Delta t/D$ = 0.0095 is used, where D is the depth of the cavity and Δt is time step ($\Delta t = 8 \times 10^{-6} s$), which ensures that the CFL number ($CFL = \frac{u\Delta t}{\Delta x}$, where u is the freestream velocity, and Δx is the grid size in streamwise direction) is less than 1 for all cases. The Reynolds number is $Re = 3.9 \times 10^5$ (corresponding to $Re = 3.9 \times 10^6$ at full scale) based on the cavity depth and the freestream properties. The number of cells for case 1, 2 and 3 are 56.2, 57.8 and 53.1 million, respectively. The reason for using a reduced scale is not to make validation against a specific model, but rather to reduce the computational demands of the mesh. The simulation results of the mean pressure coefficients C_p for an empty closed cavity case and far-field acoustic pressure spectra for raised DSA 350 pantograph have been validated against experimental data by Kim *et al.*[32,33]. Furthermore, the Reynolds numbers of all components of the raised pantographs are in the upper subcritical regimes[33]. Therefore, it may be assumed that vortex shedding and coefficient of forces remains unchanged for both pantograph and the cavity[34].

Table 2. The refinement zones and mesh criteria for each zone.

Refinement region	Number of zones	Cell size (mm)	Number of boundary layers
Cavity leading edge	1	6.0	40
Cavity trailing edge	2	1.2	40
Cavity inside	2	2.0	40
Cavity overall	5	8.0	N/A
Insulation plate edge	2	2.0	30
Raised pantograph panhead wake	4	1.0 - 1.8	N/A
Raised pantograph upper arm wake	2	1.5	N/A
Raised pantograph joint wake	1	1.5	N/A
Raised pantograph lower arm wake	1	1.8	N/A
Around pantograph components	30	0.4 - 0.8	14

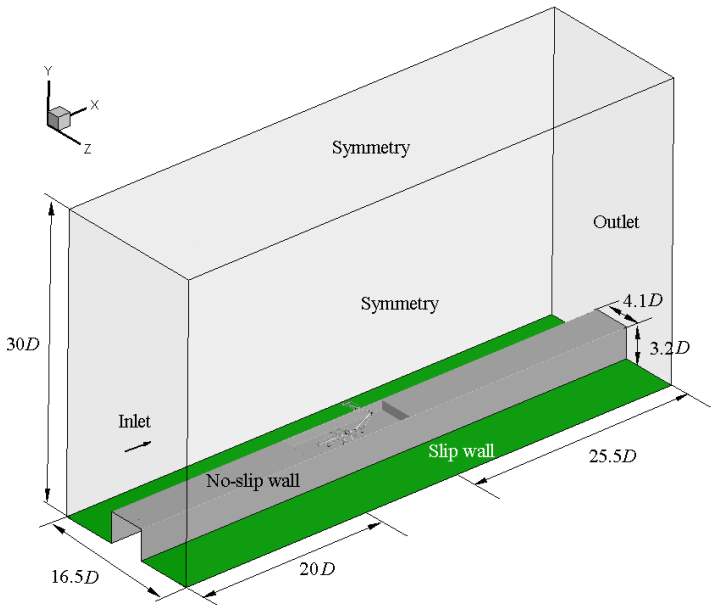

(a) Computational domain

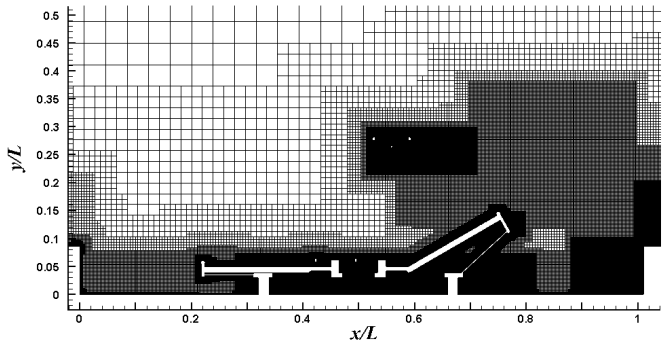

(b) Overall view of the mesh

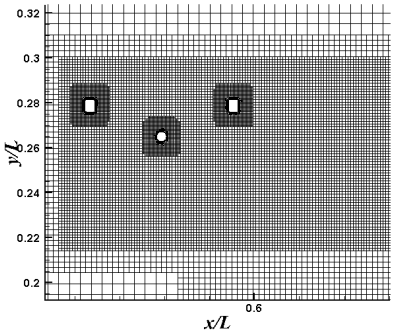

(c) Mesh around the panhead

Figure 2. Computational domain and boundary conditions, and overview and detail of the meshes.

Aerodynamic results

Forces

The mean and rms values of the coefficients of lift C_L, and drag C_D from the whole model, the raised pantograph, the folded pantograph and the roof and insulation plates are shown in Figure 3. The cavity cross section $W \times D = 0.0196\ \mathrm{m}^2$ is used as the reference area to calculate each of the force coefficients. The force coefficients were obtained after running the cases for 0.05 s when the flow is deemed to be statistically steady by checking the time history of the force coefficients. Data were then collected at each time step for 0.15 s. For all cases, the mean lift coefficients $\overline{C}_L$ of the whole system are negative. The cavity roof configuration (case 1) has the highest negative lift force. The ramped roof cavity configuration (case 2) induces a higher mean drag force coefficient $\overline{C}_D$ than cases 1 and 3 by 35% and 55% respectively. The mean drag and lift forces from the

pantographs are significantly smaller than those from the roof and insulation plates. For all cases, the mean drag force of both the raised and the folded pantographs is larger than the corresponding mean lift and side forces. Furthermore, the mean side force coefficient $\overline{C}_S$ is significantly small compared with other forces because the geometries for all cases are symmetric with respect to the central vertical plan ($z/W = 0.5$). The fluctuating lift (C_L^{rms}) and the fluctuating drag force (C_D^{rms}) for case 2 are higher than the fluctuating side force (C_s^{rms}). However, the fluctuating side force for cases 1 and 3 is slightly higher than the fluctuating lift and drag forces.

The PSDs of C_L, C_D, and C_s are displayed in Figure 4. These are obtained based on Welch's method using a Hanning window with a 50% overlap between segments and have been adjusted to full scale frequencies. For all three force spectra of the whole system, the results for cases 1 and 2 are higher than those for case 3 at low frequencies up to 200 Hz. This is due to fact that the cavity and ramped roof components are the main contributors to those force fluctuations. These are produced by large-scale flow structures at low frequency (below 200 Hz) and produce higher forces than for the side insulation plate configuration, as shown in Figure 4(j) - (l). For cases 1 and 2, a broad peak appears in the lift coefficient spectrum at 635 Hz in Figure 4(j). This peak is generated by the insulation plate edges due to vortex shedding from the plates. Comparing cases 1 and 2, the three force coefficients the spectra of the roof and the insulation are similar in most of the frequency range, except below 20 Hz where the amplitude of the spectra for case 2 is higher than for case 1. Furthermore, in the spectra of the drag force coefficient C_D of the roof and insulation plates shown in Figure 4(k), there is very large difference between case 3 and the other two cases. For the raised pantograph in Figure 4(d) and (e), there are tonal peaks at 280 Hz and 450 Hz in the spectra of the lift force, and at 270 Hz and 550 Hz in the spectra of the drag force. These peaks are associated with vortex shedding from the upstream contact strip (270 Hz) and the horn (550 Hz). These two peaks can also be seen in the spectra of far-field pressure as will be discussed later. In the side force spectrum of the raised pantograph, another tonal component at 610 Hz is produced by the horn. For all three force spectra of the folded pantograph in Figure 4(g) - (i), the spectra for case 2 are lower than those for cases 1 and 3 in the most of frequency region. The spectra for case 1 are higher than those for cases 2 and 3 at low frequencies up to 50 Hz, whereas the folded pantograph for case 3, as it is exposed in the freestream flow, has higher force fluctuations for case 3 than for cases 1 and 2 in the high frequency region, i.e. over 210 Hz for lift and drag force, and 240 Hz for side force.

Time-averaged velocity field

Figure 5 compares the profiles of streamwise velocity U_x at various streamwise locations along the middle of the train roof ($z/W = 0.5$) for the three cases, pantographs are shown to indicate the relative position. For cases 1 and 2, the incoming flow separates at the cavity leading edge ($x/L = 0$). At $0.1 < x/L < 0.3$, negative velocity appears due to the recirculation zone formed for cases 1 and 2. Compared with cases 1 and 3, lower velocity occurs for case 2 at $0 < y/L < 0.16$ between the leading edge and $x/L = 0.7$. This is because the separation flow from the leading edge produces a large recirculation region above the folded pantograph. This low velocity may reduce the noise radiated from the folded pantograph and the lower part of the raised pantograph compared with case 3 [33].

The cavity roof configuration (case 1) has the lowest incoming flow velocity at the upstream contact strip in the region $0.25 < y/L < 0.3$ due to the influence of the cavity flow [my paper], whereas the ramped cavity roof configuration (case 2) has the highest velocity, which is 7% higher than for case 1. However, in terms of the incoming flow velocity at the horn at $0.265 < y/L < 0.275$, the velocity in case 2 is the lowest and it is 20% lower than the configuration for case 3, which has the highest velocity in this region. These influences may affect the noise radiated from the panhead of the raised pantograph. This will be discussed in Section Far-field sound pressure level.

Near-wall flow pattern

When flow separation happens, the recirculating flow interacts with the wall, resulting in strong unsteady wall pressure fluctuations. Therefore flow separation and attachment can be used to identify potential noise sources [38]. The wall shear stress lines, plotted by the linear integral convolution [37], are used to identify the near-wall flow characteristics. The separation, attachment patterns and critical points are determined from the wall shear stress lines according to Lazos [38] and Perry et al. [39].

Figure 6 shows the surface flow features on the side wall including the outside of the insulation plates. For case 1, flow over the train roof separates from the cavity side edge and reattaches later, forming a recirculation region on the side wall towards the rear part of the cavity, as shown in Figure 6(a) by the reattachment line. For case 2, flow separation and attachment occur at both the upstream and downstream edges of the insulation plate. The separated flow at the upstream ramp side edges introduces strong vortices which impinge on the side wall, causing a large separation on the insulation plate. This also happens at the rear edge, where vortical flow from the ramped cavity introduces a large separation on the insulation plate. Flow separation at the front edge of the insulation plate is much smaller for case 3 than for case 2. The flow remains attached on other parts of the insulation plate surface.

These flow features over the insulation plate are shown in Figure 7 by streamlines initiated upstream from a line from (x, y, z) = (-0.2 m, 0.01 m, 0.2 m) to (x, y, z) = (-0.2 m, 0.01 m, 0.31 m). For case 1, the incoming flow in the middle of the train roof (red arrows) attaches on the cavity floor after separating from the cavity leading edge. It continues over the cavity, the insulation plate edge and reattaches on the insulation plate outside surface and merges with the flow (blue arrows) from outside the cavity. For case 2, the flow pattern is similar to case 1 for the incoming flow in the middle part of the roof (red arrows). The flow separated from the ramped roof edge (blue arrows) attaches on the side plate surface and goes inside the cavity and separates at the cavity trailing edge. In case 3, due to the absence of the

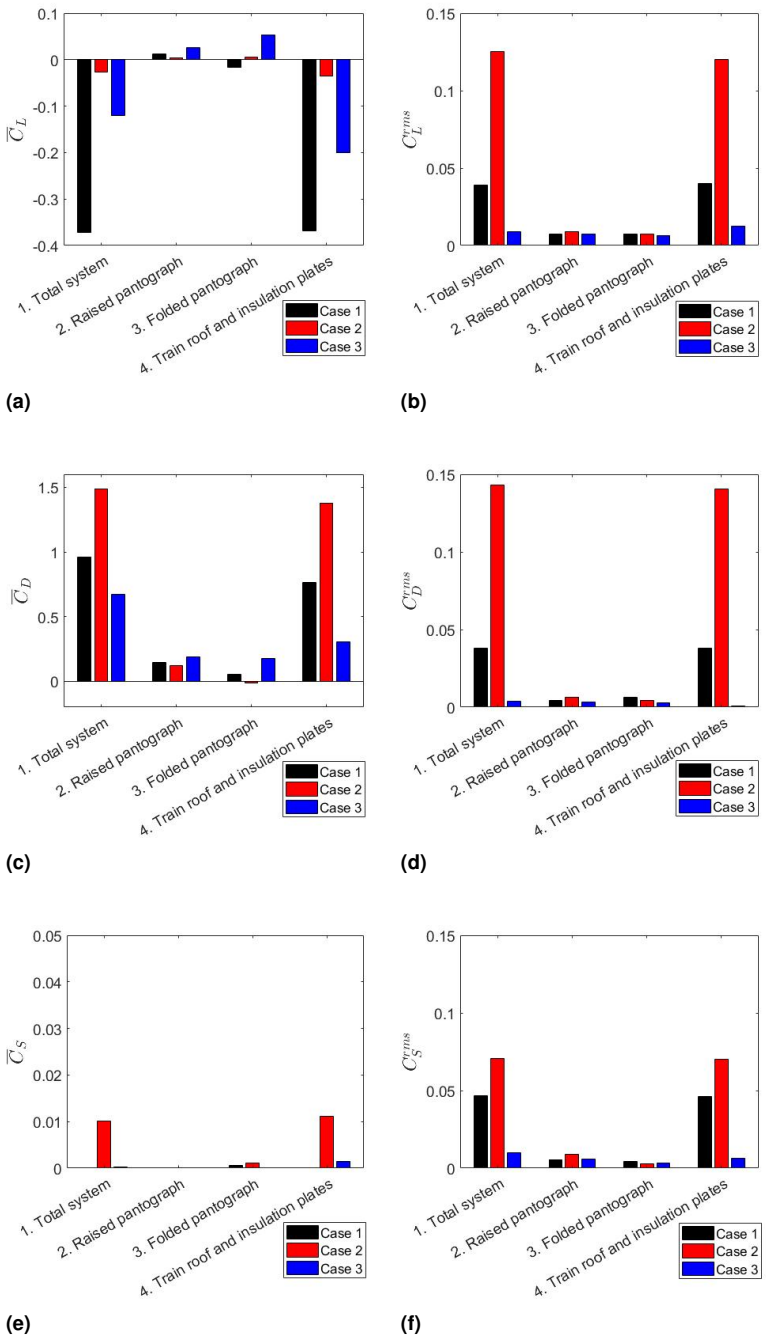

Figure 3. Force coefficients for different roof geometry configurations. (a) Mean lift coefficient $\overline{C}_L$; (b) rms lift coefficient C_L^{rms}; (c) mean drag lift coefficient$\overline{C}_D$; (d) rms drag coefficient C_D^{rms}; (e) mean side force coefficient$\overline{C}_D$; (f) rms side force coefficient C_D^{rms}

cavity, the flow is fully attached to the side plate, except for a small separation region at the insulation plate front edge (Figure 7(c)).

Figure 8 shows the near-wall surface flow patterns with critical points as defined by Lazos[38] and Perry et al.[39]. For case 1, there are two primary attachment lines on the floor and the aft wall of the cavity, as shown in Figure 8(a). The shear layer separates from the leading edge of the cavity and reattaches to the cavity floor at $x/L = 0.43$, near the rear feet of the front folded pantograph. The flow separating from the cavity trailing edge reattaches on the aft wall, forming a separation region, which is $0.6D$ long at the middle ($z/W = 0.5$) and $1.1D$ long at z/W = 0.25 and 0.75. For case 2, a favourable pressure gradient occurs in front of the upstream ramp with a stagnation point (unstable node point). The flow separated from the ramped cavity leading edge reattaches with two unstable nodes and a saddle of attachment in the middle of the cavity floor at $x/L = 0.68$. The flow separates again downstream of the cavity forming two stable focus points. This separated flow reattaches on the aft wall of the ramped cavity with two unstable node points and one saddle of attachment point. Furthermore, two separation lines are observed along the cavity side corner. For case 3, a common feature is found at the front and rear parts of the pantograph feet (cylinder) forming two corner

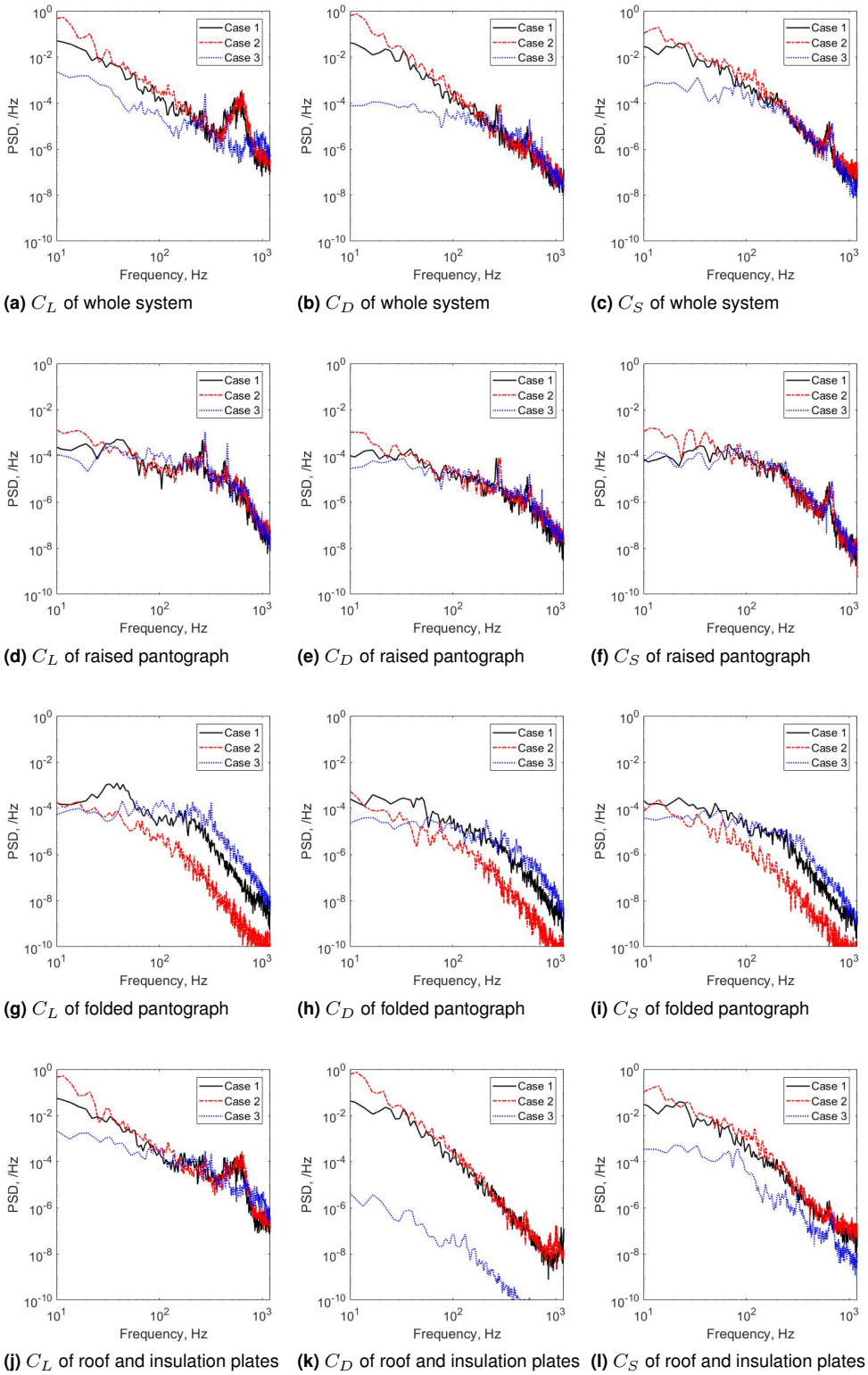

(a) C_L of whole system **(b)** C_D of whole system **(c)** C_S of whole system

(d) C_L of raised pantograph **(e)** C_D of raised pantograph **(f)** C_S of raised pantograph

(g) C_L of folded pantograph **(h)** C_D of folded pantograph **(i)** C_S of folded pantograph

(j) C_L of roof and insulation plates **(k)** C_D of roof and insulation plates **(l)** C_S of roof and insulation plates

Figure 4. PSD of force coefficients for different roof geometry configurations.

separations in which the flow structure is characterised by two saddle points (one in the front and one in the rear of the feet). Furthermore, the separation lines occur at the front and side of the feet and the attachment lines are observed at the downstream of each foot.

More detail of the flow characteristics including Q-criterion, time-averaged velocity 2D contour and surface pressure fluctuations over pantographs and recess have been presented by Kim *et al.*[40].

Aeroacoustic results

Far-field sound pressure level

Two far-field receivers are defined in the model, located at the side and one directely above the cavity with radius 2.5

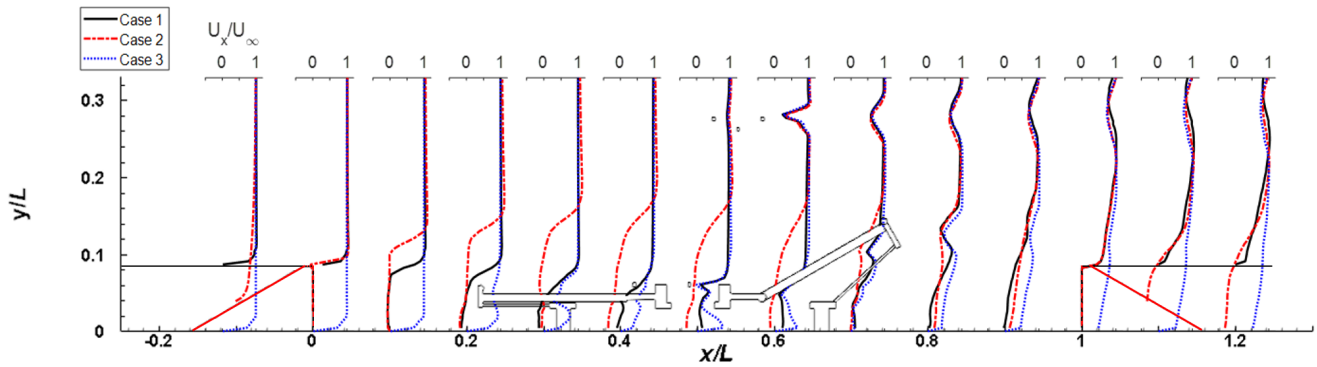

Figure 5. Time-averaged streamwise velocity over roof and pantographs.

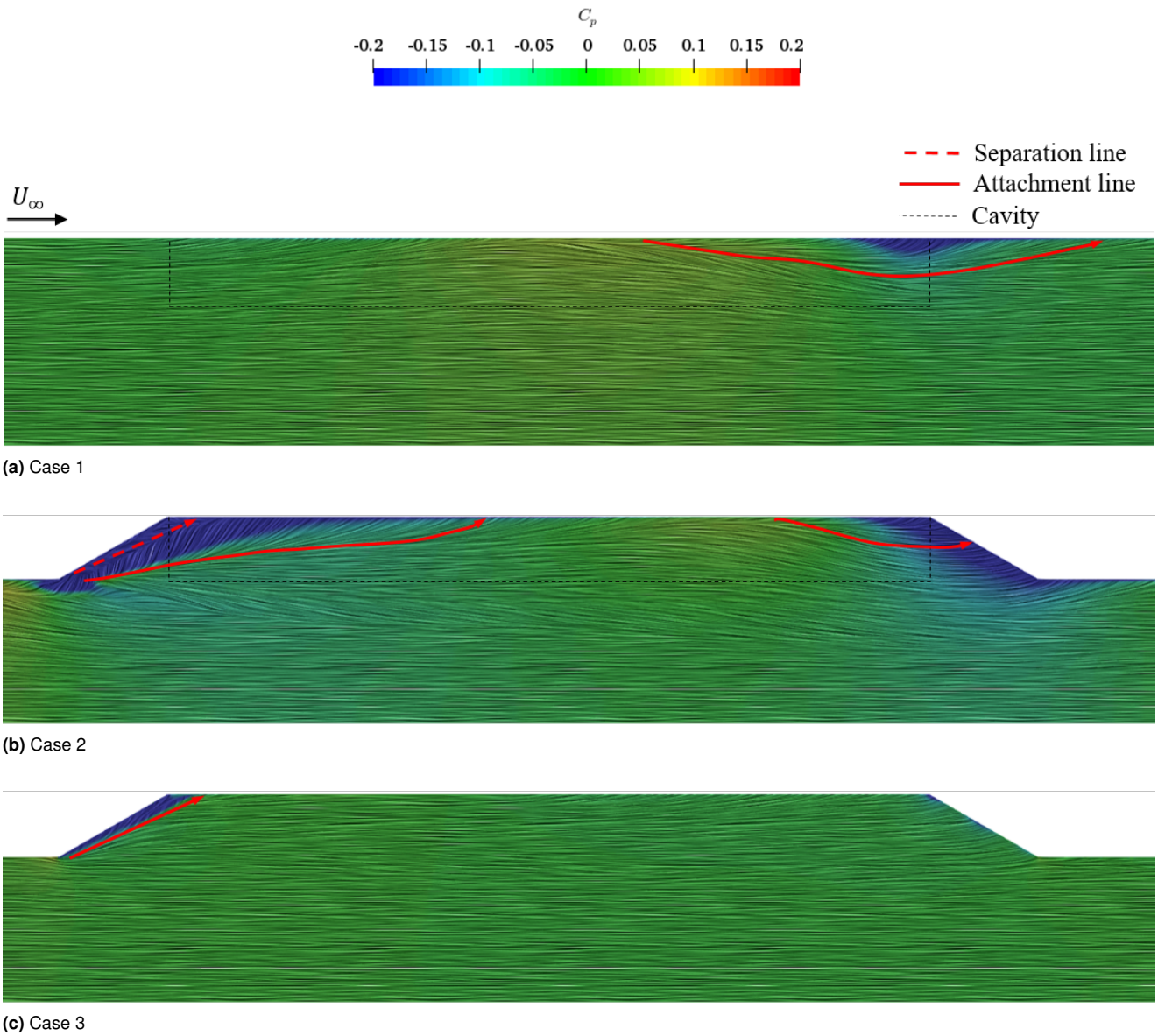

(a) Case 1

(b) Case 2

(c) Case 3

Figure 6. Mean wall shear stress lines coloured by the mean pressure coefficient.

m (corresponding to radius 25 m at full scale) centred at the middle of the cavity floor. The sampling frequency of the far-field noise was 125 kHz at 1/10 scale. A segmental average using a Hanning window with 50% overlap was used[41] to calculate the narrow band spectra, which were converted to 1/3 octave bands and adjusted to full scale using an aeroacoustics similarity law[42].

Figure 9 shows the spectra of the radiated sound pressure at a receiver directly to the side as well as the contributions from different components. The corresponding OASPL values are listed in Table 3. The SPL from the whole system for case 2 is higher in the low frequency region (below 250 Hz) than

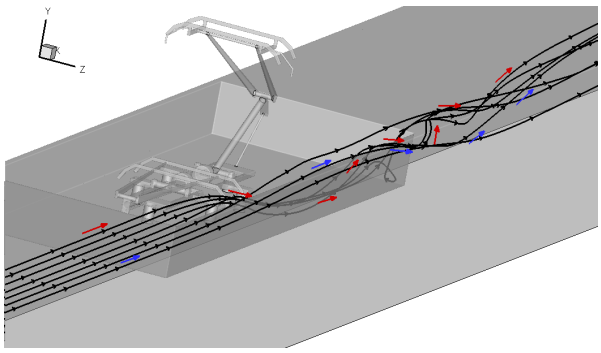

(a) Case 1

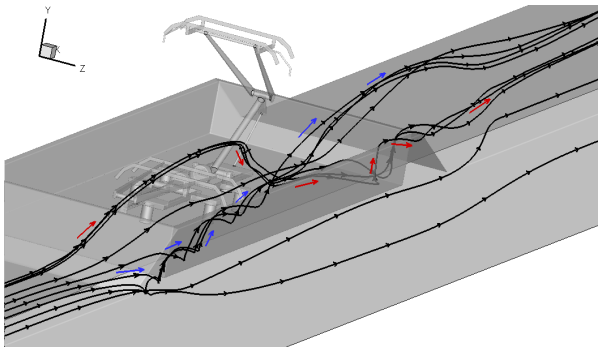

(b) Case 2

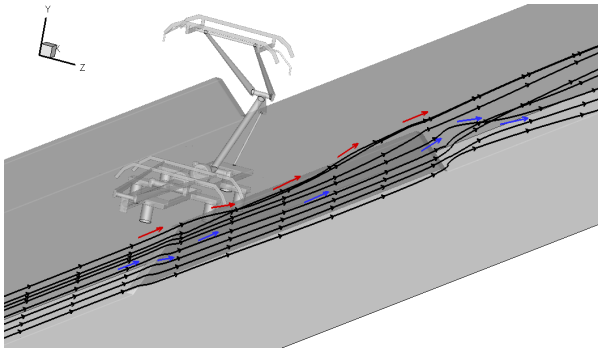

(c) Case 3

Figure 7. Time-averaged 3D streamlines for flow over the side of the train.

for cases 1 and 3, as shown in Figure 9(a). This is due to stronger noise radiation from the ramped cavity itself (see Figure 9(d)). Figure 9(b) shows the spectra of radiated noise from the raised pantograph. Two strong tonal components are seen in the 250 Hz and 500 Hz band. The first peak is associated with the upstream contact strip of the panhead and the second is generated by the horn of the panhead[5]. In general, the SPL for case 1 is slightly lower in most of the frequency range than for cases 2, and 3.

Figure 9(c) shows the spectra of the noise radiated from the folded pantograph, which are generally lower. There are no strong tonal components and the radiated noise is broadband for all cases. The noise for cases 1 and 2 is lower than for case 3, as the folded pantograph for these cases is placed inside the cavity, where the flow speed is generally much lower than the freestream velocity. The radiated noise from the folded pantograph for case 2 has the lowest level, which is 12 dB lower than for case 3 because the folded pantograph in case 2 is completely within the cavity recirculation flow region without being impinged by the shear layer from the cavity leading edge. This would be the motivation of using a ramp to redirect the shear layer.

Figure 9(d) shows the spectra of noise radiated from the train roof and the insulation plates. In the low frequency region (up to 315 Hz), the radiated noise for cases 1 and 2 is higher than for case 3. In these spectra, a peak is seen at 500 Hz for cases 1 and 2, and 630 Hz for case 3. This is generated by vortex shedding from the insulation plates. However, the folded pantograph does not have a significant contribution to the total level.

Figure 10 shows the spectra of the radiated sound pressure at a receiver directly above the configuration. In general, the SPL at this location is much higher than that at the side location, especially the sound radiated from the raised pantograph and the train roof and insulation plates (see Table 3). The second tonal peak for the raised pantograph at 500 Hz in case 3 is approximately 4 dB higher than for cases 1 and 2, as shown in Figure 10(b). In Figure 10(d), it can be seen that the noise from the train roof and insulation plates for case 3 is about 11 dB higher than at side receiver position. The

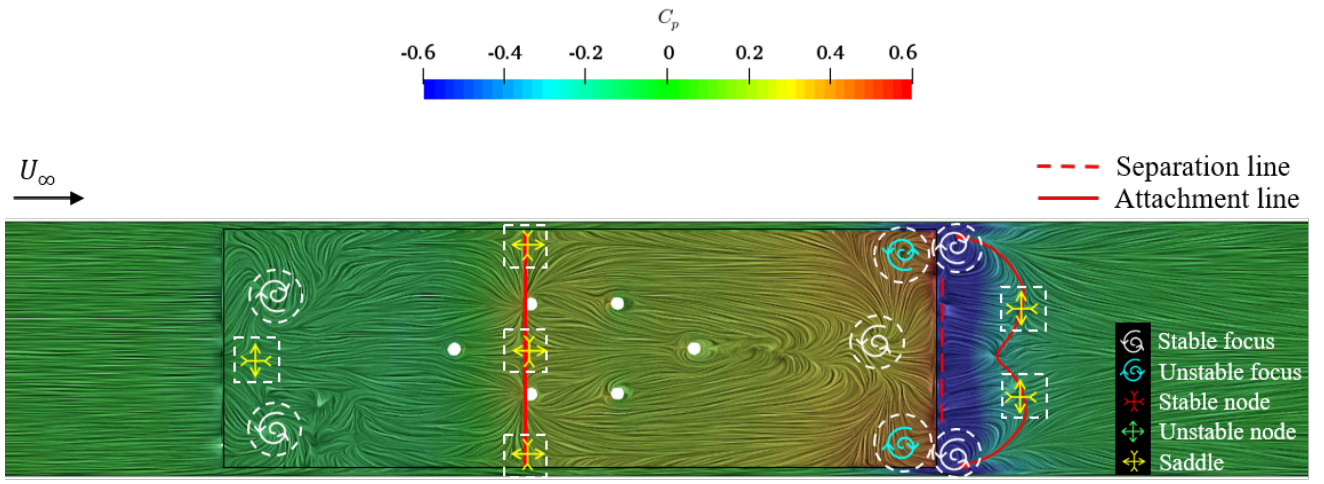

(a) Case 1

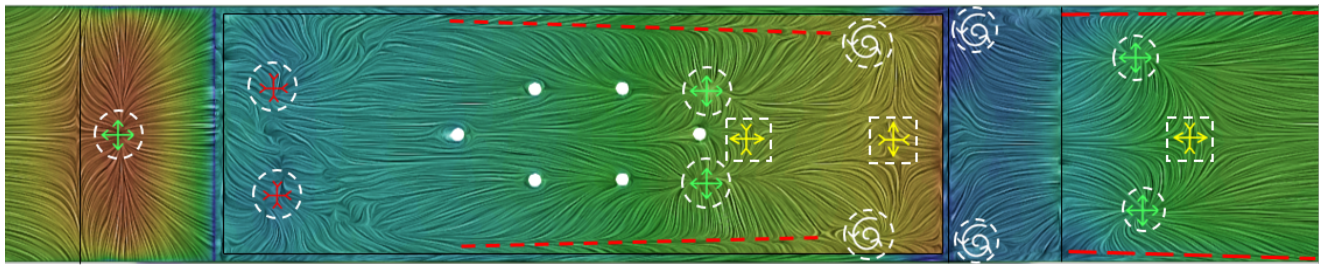

(b) Case 2

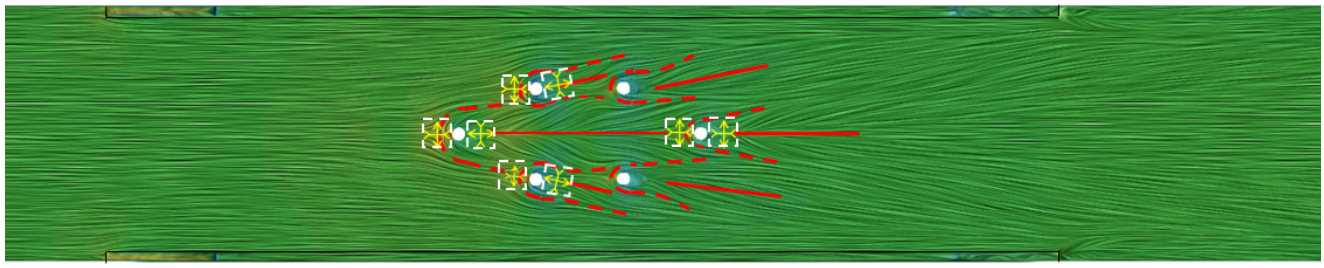

(c) Case 3

Figure 8. The wall shear stress lines coloured by the mean pressure coefficient. White circles are the feet of the pantographs.

SPL from case 3 (the insulation plate only configuration) is slightly lower in the lower frequency range below 250 Hz, whereas it is slightly higher in the high frequency region between 630 Hz and 1250 Hz.

From Table 3, it can be seen that at the side position, the OASPL from case 3 is lower than that from cases 1 and 2. However, at the top position, the OASPL from case 3 is approximately 2 dB higher than that from case 1 and 2. This is mainly due to the radiated noise from the raised pantograph, most of which is exposed to the freestream flow. The results of applying the A-weighting to the OASPL are also listed in Table 3. As the A-weighting attenuates significantly the contributions at low frequencies, the tonal peaks from the horn and insulation plate at higher frequencies become more important for the OASPL. Therefore, the A-weighted levels from case 3 become similar to those of case 2 at the side and are the highest at the top.

Conclusion

The flow and noise characteristics of three different high-speed train roof configurations including a folded and a raised pantograph have been investigated. The IDDES turbulence model is used for near field aerodynamic calculations and FW-H for far-field acoustic pressure predictions.

It is found that highly unsteady flow influence on the fluctuating forces. The fluctuating forces for ramped cavity configuration are higher than the other configurations, especially the fluctuating lift (C_L^{rms}) and the fluctuating drag force (C_D^{rms}).

Furthermore, the flow velocity inside the cavity and the ramped cavity configurations is much lower than the freestream velocity. This leads to reduced surface pressure fluctuations on both the folded pantographs and lower parts of the raised pantograph, and therefore lower radiated noise levels.

Large wall pressure fluctuations occur on the aft wall of the cavity for the roof cavity and the ramped cavity

Table 3. OASPL in dB at the side and the top.

At the side (azimuthal angle $\theta = 90°$)				
Simulation cases	Whole system	Raised pantograph	Folded pantograph	Roof and insulation plates
Case 1	90.1	85.2	77.5	89.0
Case 2	93.6	86.0	69.0	93.1
Case 3	88.5	86.4	81.7	81.2
At the top (polar angle $\phi = 90°$)				
Case 1	94.5	93.4	84.0	91.7
Case 2	94.7	94.6	70.8	92.9
Case 3	97.5	95.6	91.0	92.0
A-weighted OASPL in dB at the side (azimuthal angle $\theta = 90°$)				
Simulation cases	Whole system	Raised pantograph	Folded pantograph	Roof and insulation plates
Case 1	81.2	77.0	68.9	77.8
Case 2	83.1	78.4	57.1	81.0
Case 3	82.9	78.7	75.5	77.1
A-weighted OASPL in dB at the top (polar angle $\phi = 90°$)				
Case 1	87.8	85.0	74.9	83.7
Case 2	88.8	86.6	59.8	84.9
Case 3	91.7	88.5	84.4	86.7

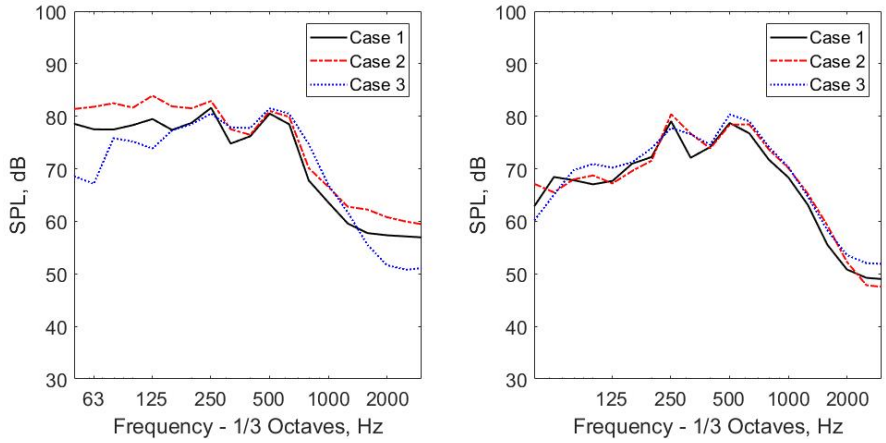

(a) Total **(b)** Raised pantograph

(c) Folded pantograph **(d)** Roof and insulation plates

Figure 9. SPL at the side receiver position.

configurations due to flow separation at the cavity trailing edge. It is also seen in slightly higher pressure fluctuations on the outside surface of the insulation plates for the ramped cavity configuration.

For the roof cavity and the ramped cavity configurations, the radiated noise level is dominated by the raised pantograph

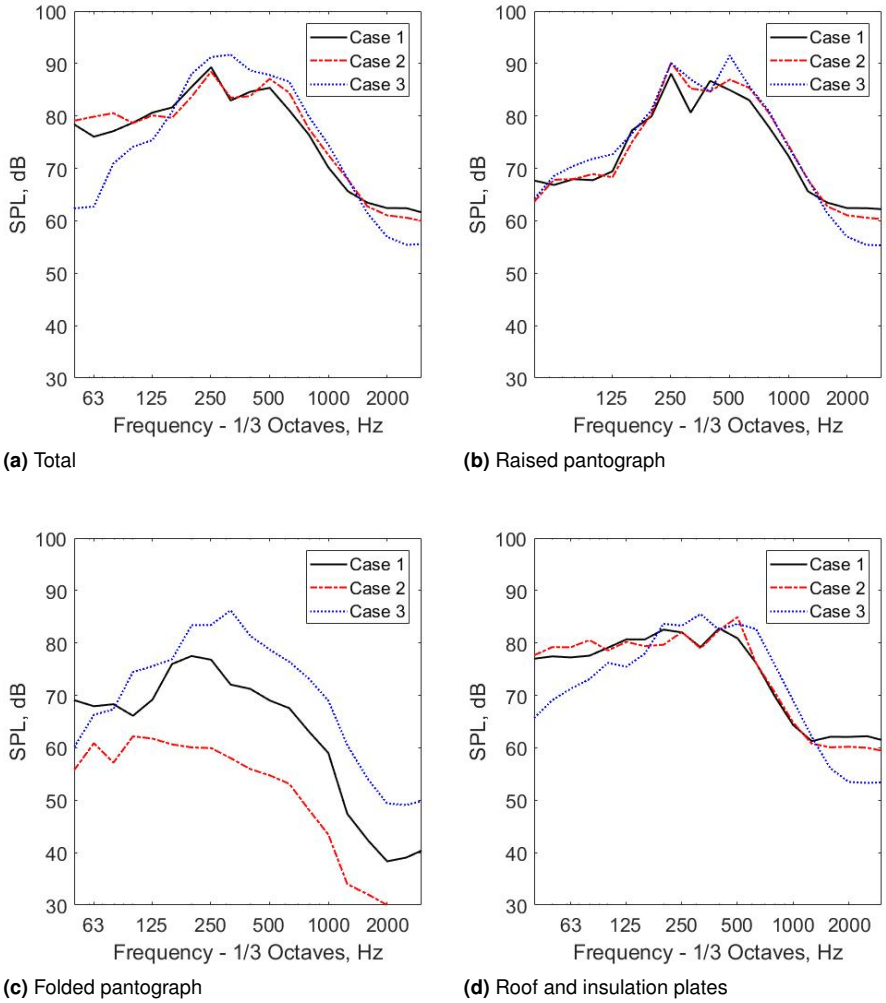

(a) Total **(b)** Raised pantograph

(c) Folded pantograph **(d)** Roof and insulation plates

Figure 10. SPL at the top receiver position.

and the roof cavity and insulation plates. The radiated noise for the ramped cavity configuration has the highest level in all directions and there is around 5 dB difference between the ramped cavity and side plate configurations at the side. The flat roof with side insulation plates has the lowest overall noise levels. However, in terms of A-weighted OASPLs, the roof configuration of only the side insulation plates has similar levels with the ramped cavity roof configuration at the side.

Acknowledgements

This research project has been supported by the Iridis 4 and Lyceum High Performance Computing Facility at the University of Southampton.

Declaration of Conflicting Interests

The author(s) declared no potential conflicts of interest with respect to the research, authorship, and/or publication of this article.

Funding

The author(s) received no financial support for the research, authorship, and/or publication of this article.

References

1. Thompson DJ. Railway noise and vibration: mechanisms, modelling and means of control. Oxford: Elsevier, 2008.
2. Talotte C. Aerodynamic noise: a critical survey. *J Sound and Vib* 2000;231(3): 549-62.
3. Talotte C, Gautier PE, Thompson DJ, et al. Identification, modelling and reduction potential of railway noise sources: a critical survey. *J Sound and Vib* 2003; 267(3): 447-68.
4. Noh HM, Choi S, Hong S, et al. Investigation of noise sources in high-speed trains. *Proc IMechE Part F: J Rail and Rapid Transit*. 2014; 228(3): 307-22.
5. Lölgen T. Wind tunnel noise measurements on full-scale pantograph models. *J ACOUST SOC AM*. 1999; 105(2): 1136. DOI: 10.1121/1.425410.
6. Grosche FR and Meier G. Research at DLR Göttingen on bluff body aerodynamics, drag reduction by wake ventilation and active flow control. *J WIND ENG IND AEROD*. 2001; 89: 1201-1218.
7. Noger C. Contribution á l'étude des phénoménes

aéroacoustiques se développant dans la baignoire et autour des pantographes du TGV. Approches expérimentale et numérique des écoulements affleurant une cavité et s non-linéaires de sillage entre deux cylindres. Ph.D. Thesis, University in Poitiers, Poitiers, France, 1999.
8. Kurita T, Hara M, Yamada H, et al. Reduction of pantograph noise of high-speed trains. *J Mech sys for Transportation and Logistics*. 2010; 3(1): 63-74.
9. Anderson Jr JD. Fundamentals of aerodynamics. New York: McGraw-Hill Education, 2010.
10. Hövelmann A. Aerodynamic investigations of noise-reducing high-lift systems for passenger transport aircraft. Diploma Thesis, Royal Institute of Technology, Stockholm, 2011.
11. Lockard DP, Choudhari MM, O'Connell MD, et al. Noise Simulations of the High-Lift Common Research Model. In *23rd AIAA/CEAS Aeroacoustics Conference* 2017, pp. 3362.
12. Wen L. Numerical Investigation of Landing Gear Noise. Ph.D. Thesis, The University of Southampton, UK, 2011.
13. Spalart PR, Shur ML, Strelets MK, et al. Towards noise prediction for rudimentary landing gear. *Procedia Engineering*. 2010; 6: 283-92.
14. Greschner B, Thiele F, Jacob MC, et al. Prediction of sound generated by a rod-airfoil configuration using EASM DES and the generalised Lighthill /FW-H analogy. *Computers & fluids*. 2008; 1; 37(4): 402-13.
15. Glegg S, Devenport W. Aeroacoustics of low Mach number flows: fundamentals, analysis, and measurement. Academic Press; 2017.
16. Paradot N, Masson E, Poisson F, et al. Aero-acoustic methods for high-speed train noise prediction. *Proc the World Congress in Railway Research*, Seoul, Korea, 2008
17. Zhu JY, Hu Z, Thompson DJ. The flow and flow-induced noise behaviour of a simplified high-speed train bogie in the cavity with and without a fairing. *Proc IMechE Part F: J Rail and Rapid Transit*, 2018; 232(3): 759-73.
18. Lockard D, Choudhari M. Noise radiation from a leading-edge slat. *In 15th AIAA/CEAS Aeroacoustics Conference* 2009; p. 3101.
19. Liu W, Kim JW, Zhang X, Angland D, Caruelle B. Landing-gear noise prediction using high-order finite difference schemes. *J. Sound and Vib*. 2013; 8;332(14):3517-34.
20. Wang M, Fattah RJ, Angland D, Zhang X. High-order hybrid cell-centered method for computational aeroacoustics. *In 21st AIAA/CEAS Aeroacoustics Conference*. 2015; p. 3279.
21. Iglesias EL, Thompson DJ, Smith MG. Component-based model to predict aerodynamic noise from high-speed train pantographs. *J Sound and Vib*, 2017; 394: 280-305.
22. Zhu C, Hemida H, Flynn D, Baker C, Liang X, Zhou D. Numerical simulation of the slipstream and aeroacoustic field around a high-speed train. *Proceedings of the Inst. of Mech. Eng., Part F: J Rail and Rapid Transit*, 2017; 231(6):740-56.
23. Spalart PR. Detached-eddy simulation. *Annu Rev Fluid Mech*. 2009; 41: 181-202.
24. Spalart PR, Deck S, Shur ML, et al. A new version of detached-eddy simulation, resistant to ambiguous grid densities. *Theor Comp Fluid Dyn*. 2006; 20(3): 181.
25. Spalart PR. Strategies for turbulence modelling and simulations. In *Eng Turb Modelling and Experiments 4* 1999, pp. 3-17, Elsevier Science Ltd.
26. Shur ML, Spalart PR, Strelets MK, et al. A hybrid RANS-LES approach with delayed-DES and wall-modelled LES capabilities. *Int J Heat Fluid Fl*. 2008; 29(6): 1638-49.
27. Lighthill MJ. On sound generated aerodynamically I. General theory. *P Roy Soc Lond. A-Math Phy*. 1952; 211(1107): 564-87.
28. Dowling AP and Williams JF. Sound and sources of sound. Ellis Horwood Ltd., Chichester: J. Wiley and Sons, 1983.
29. Ffowcs Williams JE, Hawkings DL. Sound generation by turbulence and surfaces in arbitrary motion. *Philos T R Soc Lond. A-Math Phy*. 1969; 264(1151): 321-42.
30. Brentner KS and Farassat F. An analytical comparison of the acoustic analogy and Kirchhoff formulation for moving surfaces. *The American Helicopter Society 53rd Annual Forum*, Virginia Beach, United States April 29 - May 01, 1997.
31. Brentner KS, Farassat F. Modeling aerodynamically generated sound of helicopter rotors. *Prog Aerosp Sci*. 2003; 39(2-3): 83-120.
32. Kim H, Hu Z, Thompson DJ. Effect of cavity flow control on high-speed train pantograph and roof aerodynamic noise. *Rail. Eng. Sci*. 2020; 5:1-21.
33. Kim H, Hu Z, Thompson DJ. Numerical investigation of the effect of cavity flow on high speed train pantograph aerodynamic noise. *J Wind Eng. and Ind. Aero*. 2020 1;201:104159.
34. Cooper RD. Hydrodynamic Noise, Cavity Flow. Office of Naval Research; 1960.
35. Plentovich EB, Stallings Jr RL, Tracy MB. Experimental cavity pressure measurements at subsonic and transonic speeds. Static-pressure results. NASA Langley Res. Cent., Hampton, VA, Tech. Paper-3358, December 01, 1993.
36. Kolář V. Vortex identification: New requirements and limitations. In *Int J Heat Fluid Fl*, 2007; 28(4): 638-52.
37. Carbral B and Leedom LC. Imaging vector fields using line integral convolution. In *Proceedings of the 20th annual conference on Computer graphics and interactive techniques*, Anaheim, United States, 1 Aug - 6 Aug 1992, pp.263-270. Washington: USDOE
38. Lazos B. Surface topology on the wheels of a generic four-wheel landing gear. *AIAA J*. 2002; 40(12): 2402-11.
39. Perry AE, Chong MS. A description of eddying motions and flow patterns using critical-point concepts. *Annu Rev Fluid Mech*. 1987; 19(1): 125-55.
40. Kim H, Hu Z, Thompson DJ. Numerical Investigation of the Effect of various High-Speed Train Roof Configurations on Aerodynamic Noise. In *25th AIAA/CEAS Aeroacoustics Conference* 2019 p. 2645.
41. Hu Z, Morfey CL, Sandham ND. Wall pressure and shear stress spectra from direct simulations of channel flow. *AIAA J*. 2006; 44(7): 1541-9.
42. Iida A, Otaguro T, Nagarekawa H, et al. Similarity law of aerodynamic noise generation. In *6th AIAA Aeroacoustics Conference and Exhibit conference*, Lahaina, United State, 12 June - 14 June 2000, pp.2000-2012.